Constraining and Characterizing the size of Atmospheric Rivers: A perspective independent from the detection algorithm.

[1]Lawrence Berkeley National Laboratory, Berkeley, CA, USA
[2]University of California Davis, Davis, CA, USA
[3]Indiana University Bloomington, Bloomington, IN, USA
[4]University of California Berkeley, Berkeley, CA, USA

H. A. Inda-Díaz[1,2], T. A. OBrien[3,1], Yang Zhou[1] and William D. Collins[1,4]

Key Points:

- Multiple independent estimates show atmospheric rivers size is between 7x10^{11} and 10^{13} m^2, with several orders of magnitude lower uncertainty than ARTMIP estimates
- Landfalling atmospheric rivers originating in the northwest Pacific are larger and more zonally oriented than those from the northeast Pacific
- In general, atmospheric rivers tend to decrease their size and become more meridionally oriented through their lifecycle

Corresponding author: Héctor A. Inda-Díaz, haindadiaz@ucdavis.edu

Abstract

Atmospheric rivers (AR) are large and narrow filaments of horizontal water vapor poleward transport. The size of ARs determines how much water vapor is carried from the tropics into higher latitudes, leading to extreme precipitation. Current AR detection and tracking algorithms have resulted in large uncertainty in the estimation of their sizes, with areas varying over several orders of magnitude among different detection methods. We develop and implement five independent methods to reduce the uncertainty and characterize the size of ARs that make landfall over the west coast of North America in the 1980-2017 period. ARs that originate in the northwest Pacific (WP) (100°E-180°E) have larger sizes and are more zonally oriented than those from the northeast Pacific (EP) (180°E-240°E). ARs become smaller through their lifecycle, mainly due to reductions in their width. They also become more meridionally oriented towards the end of their lifecycle. Overall, the size estimation methods proposed in this work provide a range of AR areas (between $7\text{x}10^{11}\text{m}^2$ and 10^{13} m^2) that is several orders of magnitude narrower than current methods estimation. This methodology can provide statistical constraints in size and geometry for the AR detection and tracking algorithms; and objective insight into AR size studies under climate change scenarios in the future.

Plain Language Summary

Atmospheric rivers (AR) are a meteorological phenomenon with strong horizontal water vapor poleward transport. ARs have significant impacts over the regions where they make landfall (negative and positive), particularly for west coast US water resources. AR size directly impacts on how much water vapor is carried from the tropics, and ARs are sometimes associated with extreme precipitation. There are large differences in size estimation between current detection methods, with areas varying over several orders of magnitude. Our work focuses on characterizing AR size using five different methods independent of the AR detection algorithm. We find that North America landfalling ARs originated in the North Pacific have areas between $7\text{x}10^{11}\text{m}^2$ and 10^{13} m^2 (between 1 and 11 times the area of California), and their lengths are on average four times their widths. ARs originating from the northwest Pacific (WP)(100°E-180°E) are bigger than those from the northeast Pacific (EP)(180°E-240°E). Also, WP ARs are more parallel to the equator than those from EP. Our methods provide a narrower range of size estimation than the current methods and could be used to constraint current and future AR detection methods. We present an objective methodology to quantify how AR size would vary under climate change scenarios.

1 Introduction

Atmospheric rivers (ARs) are long and narrow filaments of water vapor poleward transport from the tropics (Ralph et al., 2018; Newell et al., 1992; Zhu & Newell, 1998). Different mid-latitude continental regions around the world have large amounts of precipitation associated with atmospheric rivers (Ramos et al., 2015; Viale et al., 2018; Lavers & Villarini, 2013b; Waliser & Guan, 2017; Neiman et al., 2008). ARs are associated with up to half of the extreme events in the top 2% of the precipitation and wind distribution, across most mid-latitude regions. Moreover, landfalling ARs are associated with about 40–75% of extreme wind and precipitation events over 40% of the world's coastlines (Waliser & Guan, 2017). ARs can have both positive and negative effects in continental regions, while their absence can lead to droughts (M. D. Dettinger, 2013), many ARs can lead to flooding and other hydrological hazards (M. Dettinger, 2011; Lavers & Villarini, 2013a; Ralph et al., 2006; Ralph & Dettinger, 2011). Ultimately, atmospheric rivers have important consequences in the hydrological cycle of regions like California. They contribute to the accumulation of the snowpack and hence to the reservoir level and water availability (Goldenson et al., 2018; Guan et al., 2010; Eldardiry et al., 2019; Kim et al., 2013; Dirmeyer & Brubaker, 2007).

ARs practically carry the total meridional transport from the tropics to higher latitudes but may occupy only about 10% of the total longitudinal length (Zhu & Newell, 1998). The size of ARs determines how much water vapor is carried from the tropics into higher latitudes, that can lead to extreme precipitation. The size of an AR plays an important role in water vapor transport, extreme precipitation/wind, and hydrometeorological, social, and economic impacts. Ralph et al. (2019) introduced a scale to categorize AR strength based on vapor transport intensity and landfall duration. They show that there are beneficial and hazardous impacts associated with AR events and demonstrated the importance of studying the intensity and duration of ARs. We hypothesize that ergodicity exists between AR size and duration, and they can be equivalent; therefore, their size is directly related to the benefits and hazards associated with them. Therefore, the question "how large an atmospheric river is?" represents a key aspect of research in the atmospheric river research community.

The Atmospheric River Tracking Method Intercomparison Project (ARTMIP) has made an international effort to understand whether our scientific understanding of ARs may depend on the detection algorithm. The different ARTMIP detection and tracking algorithms are designed to answer different questions, and they produce differences in AR climatology (Shields et al., 2018; Rutz et al., 2019); therefore there are differences in their detected shape and size. It has become clear that AR detection and tracking are heavily influenced by how researchers have quantitatively identified this phenomenon, which has resulted in large uncertainty in the estimation of the size, with areas varying over several orders of magnitude among different detection methods (see Figure 1).

The definition of AR boundaries, and hence the size quantification, are ongoing research questions, and therefore the large uncertainty among methods is to be expected. Some recommendations made after the formal AR definition in the Glossary of Meteorology in 2018 were "to keep the definition as short as possible and to leave specifications of how the boundaries of an AR are to be quantified open for future and specialized developments" (Ralph et al., 2018). The research described in this manuscript works toward reducing uncertainty in the size of AR through the development and implementation of 5 independent size estimation methods. To do so, we create a North American coast landfalling winter (November-April) AR composite for the 1980-2018 period, and objectively estimate the size of ARs using the integrated vapor transport (IVT) from ERA5 reanalysis data (Copernicus Climate Change Service, 2017). These methods are not directly related to any AR detection or tracking algorithm, and we argue that they collectively provide a robust and objective way to estimate AR size.

2 Data

In this work, we use the AR detection results from three different ARTMIP Tier 1 methods (Rutz et al., 2019; Shields et al., 2018): `CASCADE_BARD_v1`(O'Brien, Risser, et al., 2020), `Lora_global`(Lora et al., 2017), and `Mundhenk_v3` (Mundhenk et al., 2016). Employing these three different detection algorithms allows us to broadly sample ARs in the north Pacific Ocean. Each of these methods generates a binary flag, 1 for "AR conditions exist", and 0 for "AR conditions do not exist", for each latitude-longitude grid point. AR binary flags for each AR were detected and tracked using thermodynamic and dynamical fields from the Modern-Era Retrospective Analysis for Research and Applications Version 2 (MERRA2) reanalysis (Gelaro et al., 2017), as a part of the ARTMIP Tier 1 catalog (Shields et al., 2018). In the methods section, we describe how we use these binary flags to create the AR composite.

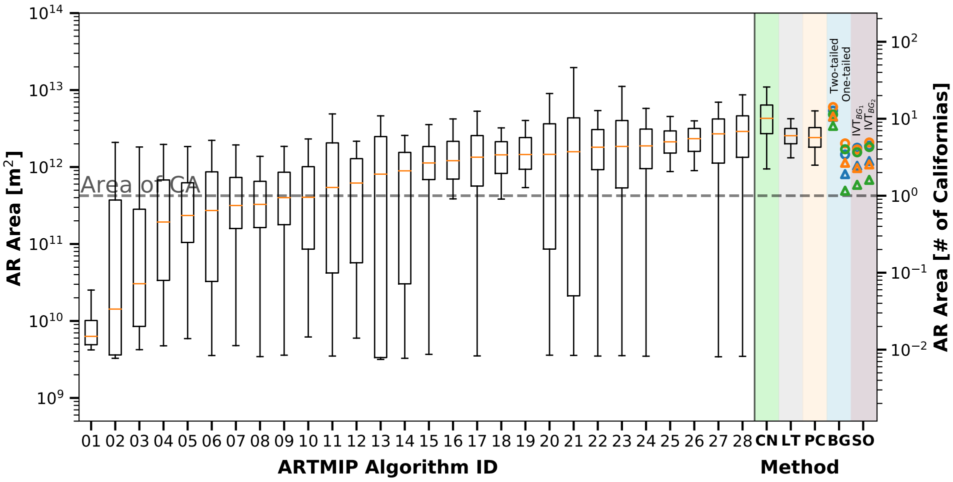

Figure 1. White background: AR area calculated from different methods in ARTMIP, ordered by median area (01-17). Colored background: AR area calculated in this work using the ClimateNet ARTMIP campaign (CN), Lagrangian Tracers method (LT), Principal Component Analysis of IVT (PC), KS-test between the IVT of AR and the background IVT field (BG), and the statistical overlapping of the conditional probability distribution of IVT given distance to the center of AR and the background IVT probability density function (SO): see Sections 3.1-3.4 for details. For BG and SO methods, triangles represent the composite of AR with northeast Pacific origin (EP) and circles represent the composite of AR with northwest Pacific origin (WP). Blue, orange, and green markers account for the 25, 50, and 75% of the AR life cycle, respectively. For the BG method, we show the results from the two-tailed and one-tailed KS-test. For the SO method, we show the results using IVT$_{BG_1}$ and IVT$_{BG_2}$, that correspond to a $p \geq \sigma^+$ at 179.5 and 193.9 kg m^{-1}s^{-1}s, respectively. (Algorithm name is included in the supporting information Table S1 for reference).

The most common variables used to characterize ARs are IVT and the column integrated water vapor (IWV). We employ the vertical integral of eastward/northward water vapour flux $[\dot{q}_x, \dot{q}_y]$ (kg m^{-1}s^{-1}), from ERA5 reanalysis, and calculate IVT as

$$\mathrm{IVT} = \sqrt{\dot{q}_x^2 + \dot{q}_y^2}, \tag{1}$$

where

$$\dot{q}_x = -\frac{1}{g}\int_{p_b}^{p_t} q\,u\,dp, \tag{2}$$

$$\dot{q}_y = -\frac{1}{g}\int_{p_b}^{p_t} q\,v\,dp, \tag{3}$$

q is the specific humidity [kg kg^{-1}], u and v the zonal and meridional wind velocity over the pressure surface p [m s^{-1}], P_b is 1000 hPa, P_t is 200 hPa, and g is the gravitational acceleration. u and v are also used in the Lagrangian tracers model used in subsection 3.3. ERA5 data have a temporal resolution of 1 hour and a horizontal resolution of 0.25 degrees. We focus our work in the 1980-2017 period from the full ERA5 reanalysis.

Following O'Brien, Risser, et al. (2020), in order to avoid the large contiguous regions of high IVT near the tropics associated with the intertropical convergence zone (ITCZ), we spatially filter the IVT field as

$$\mathrm{IVT}(x, y)' = \mathrm{IVT}(x, y) \cdot (1 - \mathrm{e}^{\frac{y^2}{2\Delta y^2}}), \tag{4}$$

where IVT'(x, y) is the filtered IVT field, x and y are the longitude and latitude, respectively, and Δy is half-width at half-maximum of the filter. We use $\Delta y = 15°$, which effectively damps the IVT to zero within the ITCZ. Hereon we refer to the filtered field as IVT for simplicity.

This analysis focuses on 37 wet seasons (November-April) in the 1980-2017 period over the North American coast. By focusing on landfalling ARs, we effectively restrain the domain to the North Pacific Basin (0°N-90°N, 100°E-240°E).

Furthermore, since the main focus of this work is to study the size of ARs, we only utilize output from the three ARTMIP algorithms to obtain a broad and robust sample of AR occurrences (time and approximate location). With the exception of the areas shown in Figure 1, we explicitly avoid using the exact shape or size determined by the detection algorithm.

3 Methods

We apply the AR life cycle tracking algorithm from Zhou et al. (2018) to the AR binary flag data (from the three detection methods used in this work) and record the position and time stamp of the detected AR. To ensure we sample over the higher possible number of ARs and avoid double-sampling events, we start by taking all the ARs detected from one tracking method. We add the ARs from the second tracking method that are not detected by the first, and finally, we add the ones from the third method that are not in the first or the second. It is essential to note that we only record the AR time stamp and centroid coordinates of each object through its life cycle (calculated using equations 8 and 8), and we do not infer the shape or size of ARs from the binary flag data. Our size-estimating methods later use the recorded AR centroid as a first guess on the time/location of an AR.

In this fashion, we create a 1980-2017 wet season (November-April) dataset of North American coast landfalling AR objects. Each object correspond to one AR, and contains the time stamp and location of the centroid through its life cycle. The dataset is divided based on AR origin location (northwest Pacific "WP" 100°E-180°E *vs* northeast Pacific "EP" 180°E-240°E); and by its AR life cycle stage, at 0.25, 0.50, and 0.75 of the AR total lifetime. All subsequent analyses and methods in this work are applied separately for each of these six sub-datasets.

3.1 Principal Component Analysis of IVT (PC Method)

Recognizing that ARs are associated with ridge-like structures in the IVT field, the principal components (PC) method is designed to estimate AR size by modeling AR shapes as Gaussian. To do this, we apply principal component analysis to the high IVT cluster closest to the centroid coordinates (or first guess). For each member of the composite, we compute the weighted covariance matrix C_w (Price, 1972) of latitude and longitude

$$C_w = \frac{\Sigma_{i=1}^{\mathrm{nx}} \Sigma_{j=1}^{\mathrm{ny}} \mathrm{IVT}_{ij} (x_{ij} - \overline{x})^T \, (y_{ij} - \overline{y})}{\Sigma_{i=1}^{\mathrm{nx}} \Sigma_{j=1}^{\mathrm{ny}} \mathrm{IVT}_{ij}}, \tag{5}$$

where x_{ij} and y_{ij} are the longitude and latitude of the ERA5 grid, $\overline{x}, \overline{y}$ are the spatial zonal and meridional mean, and the weight is given by the IVT at each grid point, $\mathrm{IVT}(x_{ij}, y_{ij})$. C_w is a 2x2 matrix, such that

$$C_w \begin{pmatrix} \vec{s}_0 \\ \vec{s}_1 \end{pmatrix} = \begin{pmatrix} \lambda_0 \, \vec{s}_0 \\ \lambda_1 \, \vec{s}_1 \end{pmatrix}, \tag{6}$$

where the eigenvectors $\vec{s}_0$,$\vec{s}_1$ are the principal components (PC) of the IVT field, and λ_0,λ_1 are the eigenvalues. The PC represent the directions of maximum variance of IVT field near the AR, and this process essentially fits a Gaussian to the IVT field. The largest eigenvalue represents the direction that explains the largest IVT variance, hence the shortest AR axis (across the AR, $\vec{s}_0$), while the smallest would represent the longest AR axis (along the AR, $\vec{s}_1$).

To filter the IVT far field we use a 2-step iterative method. First we find the IVT cluster closest to the first guess location and define the AR "core" as the points of this cluster where IVT is greater than 0.5 times the local (cluster) maximum IVT. We apply the principal component analysis to the core and use the eigenvalues and eigenvectors to create a 2D Gaussian using equation (11). Then, from the original IVT field, we filter all the points outside the 10^{-3} core Gaussian contour (we found this value worked well for smaller and larger ARs). We then apply principal components analysis to this filtered IVT field and use its results to estimate the size of the AR.

We define the width (length) of the AR as twice the magnitude of $\vec{s}_0$ ($\vec{s}_1$), and its area as the ellipse whose axes are the principal components $\vec{s}_0$ and $\vec{s}_1$ (white lines and ellipse in Figure 2). This method is labeled *PC* throughout this work. We utilize `fastKDE`[1] (O'Brien et al., 2014, 2016) to calculate probability density functions (PDF) of length, width, area and angle θ with respect to the equator.

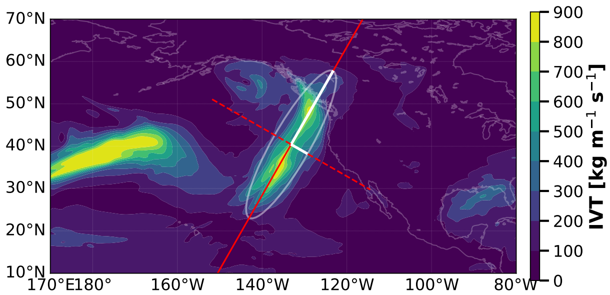

Figure 2. Principal component analysis method. White lines represent the PC of the AR, and the white contour is the area estimated from the ellipse whose axes are the PCs. The red lines represent directions along and across AR used to sample IVT for SO and BG methods (solid/dashed represent the first/second PC).

3.2 Estimating AR Size from Composites and background IVT field (BG and SO Methods)

The statistical overlapping (SO) method is used to determine the distance at which the PDF of IVT is resolvable from the background PDF. To estimate the AR length and width from the composite, we use two separate statistical methods for determining the distance at which the AR composite becomes indistinguishable from the background IVT field. The statistical overlapping (SO) looks at the overlapping between the background field PDF and AR composite as a function of the distance. On the other hand, the K–S statistic with the background IVT method (BG) looks at the difference between the background cumulative distribution function (CDF) and the conditional probability distribution of the AR composite IVT given the distance to the center. We describe both methods in §3.2.2 and §3.2.1. We calculate the AR composite area by modeling the shape of ARs as a ellipse.

[1] https://bitbucket.org/lbl-cascade/fastkde

From a total of 1150 (980) AR objects for the WP (EP) in the 1980-2017 wet seasons, we randomly sub-sample 300 events to create the AR composite. We define the AR center coordinates $(\overline{x}, \overline{y})$ for every AR event within the composite as the IVT centroid, in the same fashion as the center of mass

$$\overline{x} = \frac{\Sigma_{i=1}^{nx}\Sigma_{j=1}^{ny}\mathrm{IVT}_{ij}x_{ij}}{\Sigma_{i=1}^{nx}\Sigma_{j=1}^{ny}\mathrm{IVT}_{ij}}, \quad (7)$$

$$\overline{y} = \frac{\Sigma_{i=1}^{nx}\Sigma_{j=1}^{ny}\mathrm{IVT}_{ij}y_{ij}}{\Sigma_{i=1}^{nx}\Sigma_{j=1}^{ny}\mathrm{IVT}_{ij}}. \quad (8)$$

Then, we sample IVT along the direction of the principal components through all the domain (represented by the red lines in Figure 2), and calculate the distance d of each point to the AR center

$$d = ||(x', y') - (\overline{x}, \overline{y})||, \quad (9)$$

where (x', y') represent the coordinates of the points along the directions of the principal components. In this fashion, we create a joint distribution of IVT and d for the AR composite, and utilize `fastKDE` to calculate the conditional probability distribution of IVT given d.

We calculate the PDF and CDF of the background IVT field (which we refer to as BG) by randomly sampling IVT from ERA5 reanalysis data, through the North Pacific Ocean in the period of study. Since the definition of 'background IVT' is somewhat ambiguous, we calculate two separate backgrounds fields: IVT_{BG_1}, where the grid cells inside AR is masked at the time of sampling (using the ARTMIP binary tag for the first-guess AR detected at that time); and IVT_{BG_2}, ARs are not masked at the time of IVT sampling. Despite IVT_{BG_2} including high-IVT points inside some ARs, we remark that both backgrounds are statistically indistinguishable with a confidence level of 95% according to a two-sample Kolmogorov–Smirnov test (KS-test). The CDF of the background is higher than 0.84 ($p \geq \sigma^+$) at 179.5 and 193.9 kg m^{-1}s^{-1}s for IVT_{BG_1} and IVT_{BG_2} respectively. These two different backgrounds are used later in the SO and BG methods (described in 3.2.1-3.2.2) and referred to in the text label in Figure 1.

3.2.1 Statistical Overlapping of IVT With the Background Field PDF (SO)

One way to estimate the length and width of the AR composite is by looking at the overlap of the background IVT PDF and the composite conditional probability distribution (CPD) of IVT given distance to the center of AR. We define the statistical boundary of the AR composite as the distance where the -1-σ value (CPD(d) = 0.16) of the IVT CPD curve (lower boundary of the shading contour in Figure 3) is greater-than or equal to the +1σ value (CDF = 0.84) of the background IVT PDF (dotted line in Figure 3). In other words, we determine the AR extent by determining the distance d where the overlap between the IVT CPD and the background PDF is less than two standard deviations (the points where the dotted line intersects the lower shaded contour in Figure 3). This method is referred as SO throughout this work.

3.2.2 K-S Statistics Between AR Composite and the Background CDF (BG)

The KS-test is used to determine at which distance the CDF of the IVT is indistinguishable from the background field. We assume that the IVT distribution within AR is different from the background field.

We calculate the CDF of IVT at different distances along and across the AR composite from the conditional probability distribution of IVT given distance to the AR center. We compare the CDF of the AR against the CDF of the background IVT field (4) and apply the two-tailed and one-tailed KS-test. For the one-tailed KS-test, we define the AR

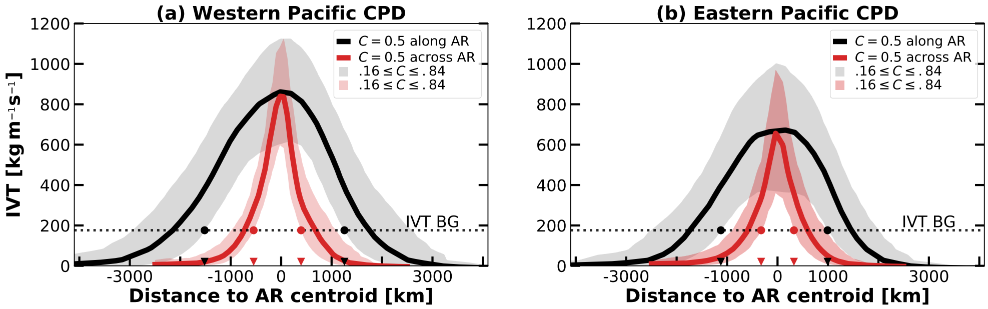

Figure 3. Conditional probability distribution of IVT given the distance to the center of the AR. Red colors represent the transverse direction (across AR), black colors represent the longitudinal direction (along AR). The 0.5 conditional probability C is represented in solid thick lines. The shading corresponds to probabilities between 0.16 and 0.84. According to the statistical overlapping method, the AR is delimited by those distances where the dashed line (background IVT $p \geq 0.84$) intersects the 0.16 CPD contour (marked in red and black dots). For example, for northwest Pacific composite (WP), approximately from -1500 to 1200 km along AR, and -600 to 400 km across AR. The triangles mark the distance of overlapping with the background.

boundaries at that distance where the CDF of the background is statistically significantly lower than the background, at the 95% confidence level. Additionally, for the two-tailed KS–test, the AR boundaries are delimited by those distances at which the KS-statistic reaches a minimum value, *i.e.* where the CDF of the AR IVT and the background field is most similar. Figure 4 shows how the CDF of the AR (in colored contours) converges to the background CDF farther from the center of AR (d = 0 km). Both BG and SO methods provide a robust statistical estimation of the AR size. They compare the conditional probability distribution of IVT (along and across AR) of the entire composite with the PDF of the background IVT. In the supplemental information we show a sensitivity test for values of AR length, width and area with changes in the background PDF and composite CPD overlapping values for the SO method, and to the statistical level of significance for the one-tailed BG method (Text S1 and Figures S1(a-b)).

3.3 Lagrangian Tracers for Area Estimation (LT)

Previous work by Garaboa-Paz et al. (2015) suggests that ARs relate to attracting Lagrangian Coherent Structures (LCS) in the 2D and 3D flow. With this in mind, we hypothesize that Lagrangian tracers can be used to estimate AR area from a fluid dynamics point of view. The association of ARs with LCS implies that tracers inside the AR are more likely to preserve spatial coherence through the backward and forward trajectory integration. Furthermore, tracers near the boundaries (and outside) of the AR would be more likely to disperse and end up at a final location farther than its initial location when compared with those inside the AR.

To do so, we use a 2D passive Lagrangian tracers advection model. The tracers are advected over pressure surfaces using 2D velocity fields from ERA5 reanalysis following the movement equation

$$dx_i = (u_i + \sqrt{2}\overline{u}_i\, w_i)dt, \tag{10}$$

where i represents the zonal and meridional directions, u the 2D velocity over pressure surfaces, $\overline{u}_i$ is the root mean square of the local velocity near the tracer (Griffa et al., 1995; Rodean, 1996; Sawford, 1991; LaCasce, 2008), and w_i is a random perturbation with zero mean and unit variance (i.e., a Wiener process). This random nudging in the tracer position at each time step is introduced to represent the diffusion, turbulence, and

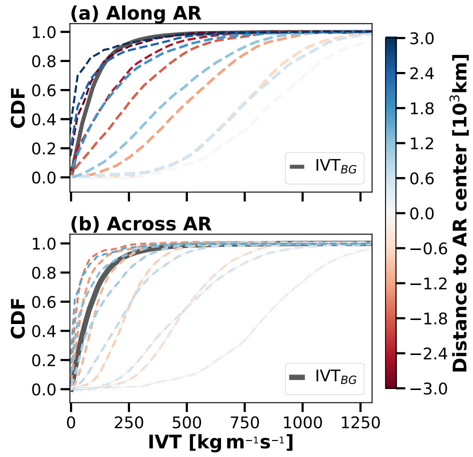

Figure 4. Colored lines show the CDF of IVT for the AR composite, at different distances from the AR center (less transparent colors represent a farther distance to the AR center). The black line shows the CDF of the background IVT field. The KS-test evaluates when the AR IVT and background fields are indistinguishable (for the two-tailed test), or the AR IVT statistically lower than the background field (for the one-tailed test).

other processes not solved by the model resolution. In the supplemental information Text S2 and Figure S2, we show a test of the sensitivity of AR area to changes of the scaling velocity $\sqrt{2\overline{u}_i}$. We solve equation (10) using the Euler method with a time-step of 1 hour (same as the ERA5 resolution, thus avoiding the need for time interpolation). The model uses bilinear interpolation in space to find the velocity at each tracer location.

We select the initial position for the tracers in the vicinity of the AR, by randomly selecting 2000 points from all the domain (-80S to 80N, 180W to 180E), with a probability given by a 2D Gaussian function centered in the AR

$$g(x, y) = \exp(-(a(x-\overline{x})^2 + 2b(x-\overline{x})(y-\overline{y}) + c(y-\overline{y})^2)), \tag{11}$$

where

$$a = \frac{\cos^2(\theta)}{2\lambda_0^2} + \frac{\sin^2(\theta)}{2\lambda_1^2}, \tag{12}$$
$$b = \frac{\sin(2\theta)}{4\lambda_0^2} - \frac{\sin(2\theta)}{4\lambda_1^2}, \tag{13}$$
$$c = \frac{\sin^2(\theta)}{2\lambda_0^2} + \frac{\cos^2(\theta)}{2\lambda_1^2}, \tag{14}$$

λ_0 and λ_1 are the eigenvalues of the covariance matrix in equation (5), $\overline{x}$ and $\overline{y}$ are the longitude and latitude of the AR center, and θ is the angle between the main axis of the AR (smallest eigenvector from equation (5) and the equator). We observe that for fewer than 500 tracers, the AR area might not be correctly resolved, since for larger AR there might be regions without tracer initial positions. For larger number of initial tracers, the initial position distribution is larger than the IVT blob. We found that 2000 tracers is in general a sufficient number for the AR within the composite and our results do not vary for larger number of initial tracers. This way, we ensure that the initial position of tracers is distributed inside and outside on the AR and around it, but no tracers (or a negligible number) far from the AR (represented by the black dots in Figure 5 (a)). Additionally, we repeat the integration 50 times for each tracer, resulting in different trajectories due to the random term in equation (10). This is equivalent to repeating the experiment 50 times, thus increasing the statistical robustness of the results. We did not find different results using a higher number of repetitions.

First, starting from the initial position, we compute the five days backward in time trajectory (resulting in the orange dots in Figure 5 (a)). Then, we use these new locations to calculate the forward in time five days trajectory (resulting in the blue dots in Figure 5 (a)). We repeat this process at each vertical pressure level in ERA5 between the surface and 500 hPa and record the tracers' final position. We choose five days because we need a timescale longer than the boundary layer and convective timescales, so we want a timescale as long as possible without exceeding the Rossby timescale by too much. Moreover, other works have found that few AR have a longer duration than five days (Zhou et al., 2018; Payne & Magnusdottir, 2016).

We calculate the PDF of the final position of the tracers (bivariate PDF of latitude and longitude), and estimate the AR area as the size of the largest contiguous contour with PDF of 0.68 (thicker green contour if Figure 5 (b)). Figure 5 (b) illustrate the idea behind this method. Supplemental information Text S2 and Figure S3 shows a test of the sensitivity of AR area relative to the changes of the PDF value used to estimate AR size.

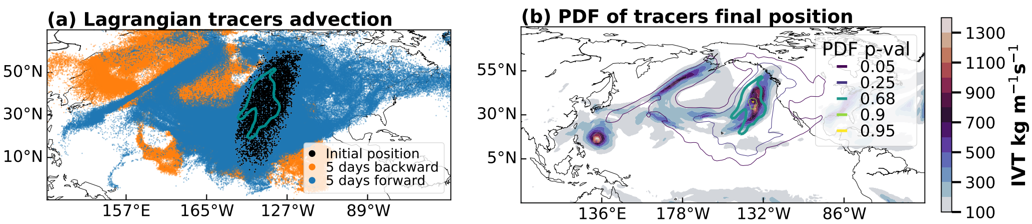

Figure 5. (a) Initial position (black), after five days backward advection (orange), and five days forward advection from the orange tracer locations (blue). The cyan contour is the 0.68 contour for the final position PDF. (b) IVT (filled contours) and PDF of the tracers' final position (contours). Thicker cyan contour at $p = 0.68$ area is used to estimate the AR size in the Lagrangian tracers method (LT).

3.4 ClimateNet method (CN)

We use *ClimateNet*[2,3] Climate Contours, which is a guided user interface for annotating climate events, facilitating the collection of hand-labeled weather datasets (Kashinath et al., 2020).

We use the data generated using ClimateNet labeling tool during the 3rd ARTMIP workshop[4] in October 2019. Half a day out of a 2.5-day workshop was devoted to this task, including over 15 workshop participants who labeled 660 time slices of data during the session (O'Brien, Payne, et al., 2020). A total of 1822 AR detections were made over the whole globe and 378 were made in the North Pacific Ocean region (which will be referred to as global and NP, respectively) using an Atmospheric Model Intercomparison Project (AMIP) simulation performed with the Community Atmosphere Model (version 5) running at 25-km resolution. We calculate the size and orientation of each of these

[2] https://www.nersc.gov/research-and-development/data-analytics/big-data-center/climatenet/
[3] http://labelmegold.services.nersc.gov/climatecontours_gold/tool.html
[4] http://www.cgd.ucar.edu/projects/artmip/meetings.html

hand-labeled ARs. Unlike the methods described in Sections 3.1-3.3, this method does not distinguish between the AR-genesis location or the life cycle.

3.5 AR Size Calculation Methods Summary

In order to aid the reader in keeping track of the various methods used in this work, Table 1 summarizes a description for each method and the short names used throughout this work.

Table 1. Methods for AR size estimation used in this work.

Method acronym	Description	Section
PC	Principal components analysis of atmospheric river integrated vapor transport field.	§3.1
SO	Statistical overlapping of AR composite conditional probability distribution of IVT given the distance to the AR center and the PDF of the background IVT field.	§3.2.1
BG	Comparison of the IVT CDF of AR composite with the CDF of the background IVT field.	§3.2.2
LT	PDF of Lagrangian tracers final position near an AR after backward and forward 5 days advection.	§3.3
CN	Hand-labeled AR using CLIMANET contours labeling tool by a group of experts at the 2019 ARTMIP workshop.	§3.4

4 Results

We focus on the size of North America landfalling atmospheric rivers. The results from all four methods in this study are consistent, with AR areas within the 10^{11} to 10^{12} m^2 range for three of the four methods: the Lagrangian Tracers (LT), KS-test with the background (BG) and the statistical overlapping (SO); and between 10^{10} to 10^{12} m^2 for the principal components method (PC). Our results have a narrower range of AR area that the ARTMIP ensemble (Figure 1), and have orders of magnitude that are consistent with the majority of the algorithms used in ARTMIP. Table 2 contains a summary of the length, width, and area for all four methods, depending on the AR genesis location and life cycle.

4.1 AR length and width

Figure 6 (a-c) show the PDF of length and width calculated using the PC method. The PDF exhibits the typical "long and narrow" shape of AR, from 2.3 to 4.5 times longer than the width (Table 3). The PC method results in a median width of 844 km (90% of the cases were between 520 and 1386 km), and length of 3842 km (90% between 2495 and 5816 km) for the AR with WP origin; and median width of 814 km (90% of the cases were between 6477 and 1476 km), and length of 3413 km (90% between 2321 and 5400 km) for the ARs with EP Origin.

For the PC method, WP has larger and wider AR than EP. The differences in length are statistically significant at a 99% confidence level, however differences in width are not. Concerning the life cycle, WP composite has the smallest AR size at 25% and the largest at 50% of its life cycle, nevertheless only the differences in length are statistically significant. The EP composite length does not change much through the life cycle. However, the width decreases monotonically through its life cycle, with differences statistically significant at a 99% confidence level.

Consistently with PC, BG, and SO methods show larger AR originated in the WP. The BG method's composite length (width) at 50% lifecycle are 4019 (1121) km for the WP, and 3275 (501) km for the EP. The SO method's composite length (width) at 50% lifecycle are 2751 (916) km for the WP, and 2107 (646) km for the EP.

The length calculated by the BG and SO methods exhibits little variation throughout the life cycle. In contrast, AR width decreased by a factor of 0.67 (WP) and 0.60 (WP) for the BG method, and 0.85 (WP) 0.69 (EP) for the SO method. These results suggest that the difference in AR size comes mainly from differences in width.

4.2 AR area

Figure 6 (d-e) shows the PDF of the AR area, calculated using the PC method (solid lines) and the LT method (dashed lines). For the WP composite, the area calculated by the PC and LT methods have a median of 2.47x10^{12}m^2 and 2.75x10^{12}m^2 respectively. For the EP composite, the area has a median of 2.23x10^{12}m^2 and 2.33x10^{12}m^2 (PC and LT respectively). The WP composite has larger areas than the EP at a 99% confidence level. EP ARs do not show a significant difference in the area through the life cycle, while WP ARs attain maximum area at their mid-life cycle for both the PC and LT methods.

The one-tailed KS-test (one-tailed BG) resulted in AR areas of 3.67x10^{12}m^2 and 1.40x10^{12}m^2 for WP and EP respectively (at 50% life cycle). The SO method calculates areas of 1.75x10^{12}m^2 and 8.74x10^{11}m^2 for WP and EP respectively (at 50% life cycle), with more extensive (both width and length) AR from WP when compared with the EP AR.

Using the BG method, AR composite area decreases through the lifecycle by a factor of 0.68 and 0.54 for the WP and EP, respectively. This change comes mainly from differences in width. The SO method shows that the composite area decreases through the AR lifecycle by a factor of 0.83 for the WP, and 0.62 for the EP.

The AR area calculated from the ARTMIP workshop ClimateNet session data has a median of 3.34x10^{12}m^2 (90% of data between 6.15x10^{11} and 7.70x10^{12}m^2) in the North Pacific region. Figure 7(a) shows larger AR areas for the global analysis 4.29x10^{12}m^2 (90% of data between 9.43x10^{11} and 1.09x10^{13}m^2). All the other methods (PC, LT, BG, and SO) are consistent with the experts' hand-labeled AR sizes, demonstrating that these methods give reasonable estimates of the composite AR area. If so, our results using ClimateNet might be on the larger side in terms of AR area, which could be related to the specific shapes the user can determine, or where the user exactly locates the AR "boundary" polygon at the time of labeling, however, these details are outside of the scope of this study.

The sensitivity tests (supplemental information Text S1 and S2, and Figures S1 to S3) show that for the SO method, variations in the overlapping background PDF and composite CPD values from (PDF, CPD)=(0.05,0.95) (minimum overlapping) to (PDF, CPD)=(0.5,0.5) (large overlapping) result in area changes from 2.84x10^{11} to 9.97^{12} m^2. BG one-tailed method sensitivity to the statistical significance level (p = 0.8 to p = 0.99) show a change in AR area from 2.26^{12} to 1.48^{12} m^2. For both BG and SO methods, AR length shows more sensitivity to variations in the parameters than width.

The sensitivity test for the LT method shows that when we use 0.68 as the PDF contour to define AR size, variations in the scaling velocity (from 0.125 times to 4 times $\sqrt{\overline{u}}$) result in an area change from 1.53^{12} to 4.16^{12} m^2. Variations in the PDF value that defines the AR area (from 0.4 to 0.93) result in area variations between one and two orders

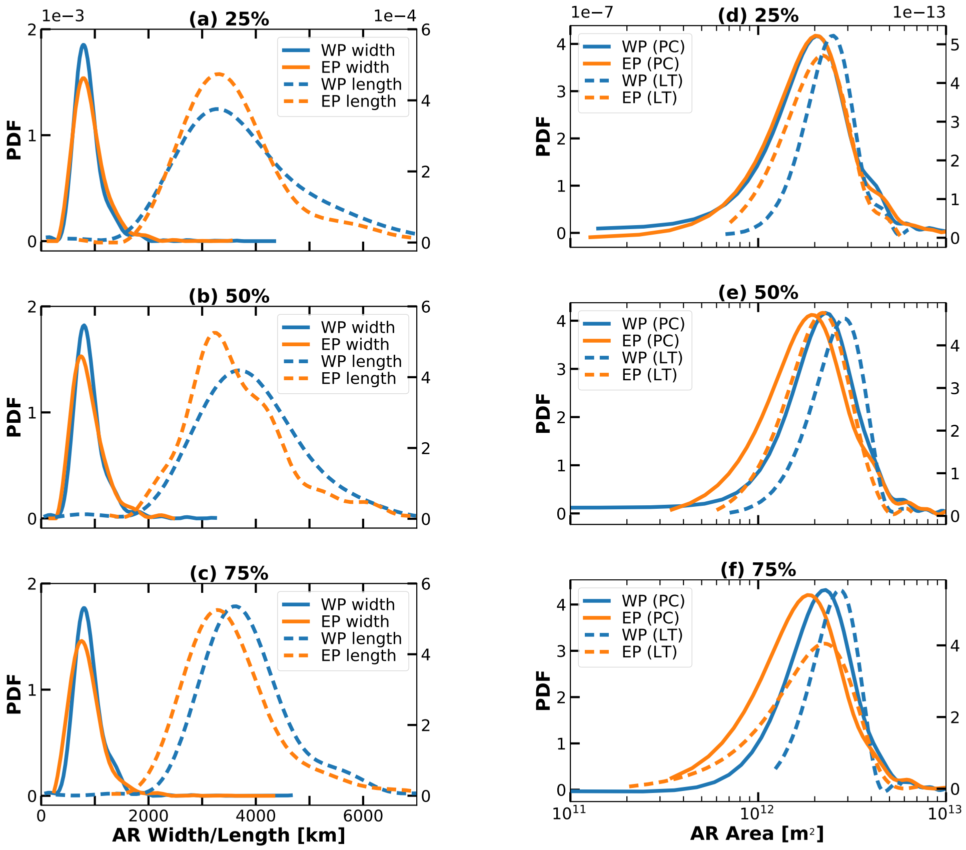

Figure 6. (a-c) PDF of AR length (dashed lines) and width (solid lines) using the principal components method (PC), at 25, 50, and 75% of the AR life cycle. WP composite in blue lines, EP composite in orange lines. (d-f) PDF of AR area for the PC method in solid lines, and the LT method in dashed lines. Lines colors same as in (a-c).

of magnitude. All the sensitivity analysis described here are for the WP at 50% life cycle. We find similar results for different stages of the AR life cycle, and for EP ARs.

4.3 AR orientation

Figure 7(b) shows the PDF of the AR orientation with respect to the equator, calculated from the principal components method (PC), and ClimateNet method (CN). PC method shows that AR originated in the WP have a more zonal orientation with respect to EP. WP orientation has a median of 13.7° (with 90% of the data between 7.7° and 99.8°). EP has a median of 49.1° (with 90% of the data between 10.4° and 142.6°). The ClimateNet method (CN) analysis for the angle of orientation has a median of 26.5° (with 90% of the data between 6.9° and 157.2°), for the North Pacific AR.

Concerning the AR lifecycle, both the WP and EP show an increase in the median angle of orientation: from 28° to 37° for the WP, and from 46° to 53° for the EP.

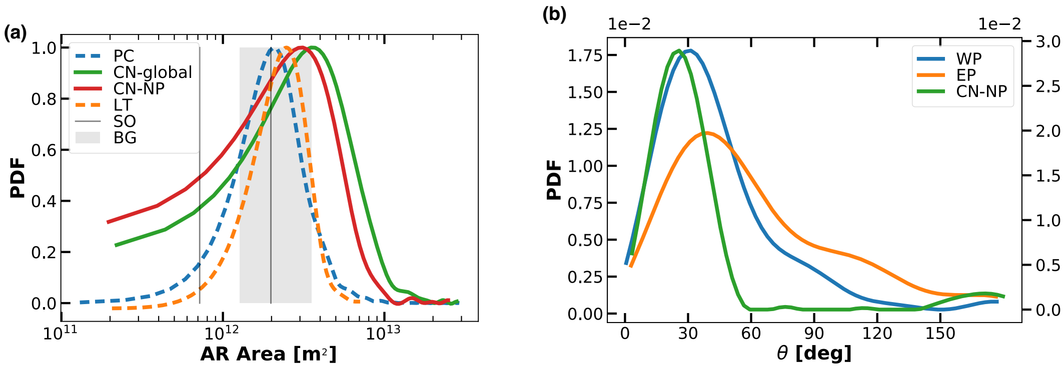

Figure 7. (a) PDF of AR area (not normalized for visualization). PC and LT methods PDF is calculated using data from WP and EP at 50% lifecycle. BG (SO) lowest to highest obtained value is represented in the shaded grey area (between solid grey lines) for comparison. (b) PDF of AR orientation with respect to the equator from the principal components method (PC), at (a) 25, (b) 50, and (c) 75% of the AR life cycle. WP composite in blue lines, EP composite in orange lines.

5 Discussion and Conclusions

Table 2 summarizes the length, width, and area of the AR composite from all the methods in this work. In previous work, two main areas of AR-genesis have been identified: over the subtropical Northwest Pacific and the Northeast Pacific (Zhou et al., 2018; Sellars et al., 2017). Here, we find robust evidence of a statistically significant difference in size, depending on their region of AR-genesis, with longer and broader ARs from the Northwest Pacific relative to those originating over the Northeast Pacific. This result may be related to the dynamical process driving the AR formation. It has previously been suggested (Zhou & Kim, 2019; Cordeira et al., 2013; Li & Wettstein, 2012) that WP atmospheric rivers have a stronger association with a thermally driven jet over the North Pacific Ocean; while EP atmospheric rivers are thought to be more associated with extratropical cyclone activity and to the commonly known phenomenon “Pineapple Express”. We also found evidence WP ARs tend to have more zonal orientation than those originating in the EP, which we believe could also relate to the dynamical feature driving the AR. This difference in AR size between the EP and WP may have implications for where meridional moisture transport occurs.

AR geometrical characteristics (aspect ratio and orientation) are summarized in Table 3. PC, BG, and SO methods agree on the typical “long and narrow” shape from the AR literature, with a median aspect ratio of approximately 4 (length/width). Other detection algorithms could use these findings as geometrical constraints in the future. The AR orientation difference between WP and EP could also directly affect the precipitation associated with landfalling AR, depending on the relative angle to the coastal mountain range, and hence the orographic lifting (Hu et al., 2017). More meridionally oriented AR towards the end of the lifecycle might modify the impacts over the coast. Furthermore, the angle of orientation of ARs increases during the lifecycle, which could be due to the tendency for ARs to eventually be entrained in the southerly flow on the northeast flank of extratropical cyclones. If there is a relationship between size, duration, propagation speeds, and orientation, this could influence the angle of AR landfalling and precipitation, which is a question worthy of further investigation.

It is worth noticing that the AR width for the end of life cycle (75%) EP composite obtained from SO and BG methods (355 and 394 km respectively) is in good agreement with airborne and satellite observations from the 1997/1998 winter ARs, where they find

Table 2. Summary of AR size statistics by method.

	Northwest Pacific			Northeast Pacific		
	0.25	**0.5**	**0.75**	**0.25**	**0.5**	**0.75**
Method	**Length** [km]					
PC	3553	3842	3757	3366	3413	3425
5-95%	2168-5984	2495-5816	2608-5562	2239-5596	2321-5454	2315-5400
BG	2783	2932	2813	2431	1640	1764
SO	2422	2650	2532	1986	1944	1580
Method	**Width** [km]					
PC	823	844	838	845	814	809
5-95%	520-1386	530-1405	510-1366	513-1550	477-1476	454-1516
BG	664	912	769	465	882	355
SO	850	812	771	625	582	394
Method	**Area** [10^{12} m^2]					
PC	2.32	2.60	2.49	2.26	2.24	2.19
5-95%	1.02-5.29	1.23-5.22	1.26-4.98	1.03-5.30	1.03-5.09	0.97-5.22
LT	2.55	2.91	2.74	2.35	2.34	2.32
5-95%	1.52-4.54	1.49-4.47	1.59-3.88	1.26-4.32	1.25-3.97	1.09-4.01
BG	1.45	2.10	1.70	0.88	1.13	0.49
SO	1.61	1.69	1.53	0.97	0.89	0.48
CN	3.34					
5-95%	0.61-7.70					

an average width scale based in IWV of 417.3 km (Ralph et al., 2004). Moreover, our result on orientation of EP ARs at the end of the life cycle (53.6 °) agree with the 17-case composite observation from dropsondes, where they find an average wind direction of the low-level jet of 216.7° (corresponding to 53.3 from our methodology's frame of reference).

We also observe a monotonic decrease in AR width through the lifecycle, which could be a systematic loss of moisture, or be associated with frontogenesis and sharpening of the frontal zone. These results could be explored in future studies, especially ones using a tracer technique.

The sensitivity tests suggest that length is more sensible than width to the choice of parameters in the statistical size estimation methods (SO and BG). We hypothesize that this is related to the difficulty to statistically distinguish the tail (or southwest end) of AR from the high water vapor and IVT near the ITZC. We observe (in a case by case exploration) that sometimes the IVT field does not have a clear boundary with respect to the ITZC, and a noisier CPD in the left side of the AR composite for large probability contours ($C > 0.9$). It is possible that this would also have an impact in the detection and tracking algorithms and their ability to objectively determine the AR boundary.

Furthermore, this raises the question about a possible link between AR size and duration, and how the size of AR might be directly related to hydrological impacts over landfalling regions. Do we need to explicitly include size in addition to IVT intensity and duration in the categorization scale for AR (Ralph et al., 2019) and their impacts? We often assume ergodicity, but if larger ARs would have systematically slower/faster propa-

Table 3. Summary of AR geometry statistics by method.

	Northwest Pacific			**Northeast Pacific**		
	0.25	**0.5**	**0.75**	**0.25**	**0.5**	**0.75**
Method	**Aspect ratio** [width/length]					
PC	4.2	4.5	4.4	3.9	4.2	4.3
5-95%	2.3-7.6	2.3-7.7	2.6-7.3	2.3-7.1	2.3-7.4	2.4-7.5
BG	4.1	3.2	3.6	5.2	1.8	4.9
SO	2.8	3.2	3.2	3.1	3.3	4.0
Method	**Orientation** [deg]					
PC	28.9	29.5	35.7	49.9	53.1	53.6
5-95%	8.1-80.2	7.3-89.2	8.5-111.8	9.5-136.5	12.3-130.1	12.1-149.6
CN	26.5					
5-95%	6.9-157.2					

gation speeds, then the AR size-life cycle (and possibly landfalling duration) relationship would not be ergodic. Our future research will work toward answering these questions.

In Figure 1 (white background part), we can observe a high spread on the size of AR among methods. Our results show values with much less spread (colored background part in Figure 1) relative to the current methods (white background part in Figure 1). This approach can provide a statistical constraint in AR size for other detection methods, and we could incorporate size into the categorization and extreme wind and precipitation impact of AR in coastal regions.

We speculate that different algorithms within ARTMIP detect different parts of the AR since each algorithm defines different rules and relatively-unconstrained thresholds. For example, since algorithms 01 to 04 are outside the range of areas estimated in this study, we can confidently argue that these algorithms are not detecting the same part of ARs as our methods or as algorithms 11-17. The AR research community may need to define more than one term, with different definitions depending on what particular meteorological feature of AR is studying. We propose three potential new terms: "AR core" (algorithms 1-4), "dynamical envelope" (LT method and maybe 9-17 methods), and "thermodynamic envelope" (PC, BG, SO, CN and algorithms 9-17). Although the dynamical and thermodynamical envelopes are indistinguishable here, they may not be in studies of future AR size. This could help understanding what is the extent of the consistency in AR detection among different algorithms, particularly the size.

We will continue to examine the relation between AR size and duration. Moreover, the direct relationship we found between AR origin location and size, the life cycle and size, motivates us to apply our methodology to understand how the AR size would change under global warming scenarios. Current detection methods may require adjusting the parameters and thresholds when studying different climate scenarios, making the objective study of change in AR size a challenging problem for future projections. Our approach could provide an objective insight into the possible changes and hydrological impacts due to AR size and climate change.

Acknowledgments

This research was supported by the Director, Office of Science, Office of Biological and Environmental Research of the U.S. Department of Energy Regional and Global Climate Modeling Program (RGCM) and used resources of the National Energy Research Scientific Computing Center (NERSC), also supported by the Office of Science of the U.S. Department of Energy under Contract No. DE-AC02-05CH11231. ERA5 is publicly available at the Copernicus Climate Change Service (C3S) Climate Data Store (CDS) - `https://cds.climate.copernicus.eu/cdsapp#!/dataset/reanalysis-era5-pressure-levels?tab=form`.

We would like to acknowledge the ClimateNet team who facilitated the labeling tool and data for the ARTMIP workshop AR labeling campaign. In alphabetical order: Karthik Kashinath, Sol Kim, Jiayi Chen, and Kevin Yang.

We would like to acknowledge the ARTMIP workshop ClimateNet AR labeling campaign. In alphabetical order: Alan Rhoades, Allison Michaelis, Ashley Payne, Brian Kawzenuk, Eric Shearer, Huanping Huang, Jonathan Rutz, Paul Ullrich, Sol Kim, Swen Brands, Yang Zhou, and Zhenhai Zhang.

References

Copernicus Climate Change Service. (2017). *ERA5: Fifth generation of ECMWF atmospheric reanalyses of the global climate.* Retrieved from `https://cds.climate.copernicus.eu/cdsapp#!/home`

Cordeira, J. M., Martin Ralph, F., & Moore, B. J. (2013). The development and evolution of two atmospheric rivers in proximity to western north pacific tropical cyclones in october 2010. *Monthly Weather Review*, *141*(12), 4234–4255. doi: 10.1175/MWR-D-13-00019.1

Dettinger, M. (2011). Climate change, atmospheric rivers, and floods in California - a multimodel analysis of storm frequency and magnitude changes. *Journal of the American Water Resources Association*, *47*(3), 514–523. doi: 10.1111/j.1752-1688.2011.00546.x

Dettinger, M. D. (2013). Atmospheric Rivers as Drought Busters on the U.S. West Coast. *Journal of Hydrometeorology*, *14*(6), 1721–1732. doi: 10.1175/jhm-d-13-02.1

Dirmeyer, P. A., & Brubaker, K. L. (2007). Characterization of the Global Hydrologic Cycle from a Back-Trajectory Analysis of Atmospheric Water Vapor. *Journal of Hydrometeorology*, *8*(1), 20–37. doi: 10.1175/jhm557.1

Eldardiry, H., Mahmood, A., Chen, X., Hossain, F., Nijssen, B., & Lettenmaier, D. P. (2019). Atmospheric River–Induced Precipitation and Snowpack during the Western United States Cold Season. *Journal of Hydrometeorology*, *20*(4), 613–630. doi: 10.1175/jhm-d-18-0228.1

Garaboa-Paz, D., Eiras-Barca, J., Huhn, F., & Pérez-Muñuzuri, V. (2015). Lagrangian coherent structures along atmospheric rivers. *Chaos: An Interdisciplinary Journal of Nonlinear Science*, *25*(6), 063105. Retrieved from `https://doi.org/10.1063/1.4919768` doi: 10.1063/1.4919768

Gelaro, R., McCarty, W., Suárez, M. J., Todling, R., Molod, A., Takacs, L., ... Zhao, B. (2017). The modern-era retrospective analysis for research and applications, version 2 (merra-2). *Journal of Climate*, *30*(14), 5419-5454. Retrieved from `https://doi.org/10.1175/JCLI-D-16-0758.1` doi: 10.1175/JCLI-D-16-0758.1

Goldenson, N., Leung, L. R., Bitz, C. M., & Blanchard-Wrigglesworth, E. (2018). Influence of atmospheric rivers on mountain snowpack in the western United States. *Journal of Climate*, *31*(24), 9921–9940. doi: 10.1175/JCLI-D-18-0268.1

Griffa, A., Owens, K., Piterbarg, L., & Rozovskii, B. (1995). Estimates of turbulence parameters from lagrangian data using a stochastic particle model. *Journal of Marine Research*, *53*(3), 371-401. Retrieved from `https://www.ingentaconnect.com/content/jmr/jmr/1995/00000053/00000003/art00003` doi: doi:10.1357/0022240953213151

Guan, B., Molotch, N. P., Waliser, D. E., Fetzer, E. J., & Neiman, P. J. (2010). Extreme snowfall events linked to atmospheric rivers and surface air temperature via satellite measurements. *Geophysical Research Letters*, *37*(20), 2–7. doi: 10.1029/

2010GL044696
Hu, H., Dominguez, F., Wang, Z., Lavers, D. A., Zhang, G., & Ralph, F. M. (2017, 04). Linking Atmospheric River Hydrological Impacts on the U.S. West Coast to Rossby Wave Breaking. *Journal of Climate*, *30*(9), 3381-3399. Retrieved from https://doi.org/10.1175/JCLI-D-16-0386.1 doi: 10.1175/JCLI-D-16-0386.1
Kashinath, K., Mudigonda, M., Kim, S., Kapp-Schwoerer, L., Graubner, A., Karaismailoglu, E., . . . Collins, W. (2020). ClimateNet: an expert-labelled open dataset and Deep Learning architecture for enabling high-precision analyses of extreme weather. *Geoscientific Model Development Discussions*(April), 1–28. doi: 10.5194/gmd-2020-72
Kim, J., Waliser, D. E., Neiman, P. J., Guan, B., Ryoo, J. M., & Wick, G. A. (2013). Effects of atmospheric river landfalls on the cold season precipitation in California. *Climate Dynamics*, *40*(1-2), 465–474. doi: 10.1007/s00382-012-1322-3
LaCasce, J. (2008). Statistics from lagrangian observations. *Progress in Oceanography*, *77*(1), 1 - 29. Retrieved from http://www.sciencedirect.com/science/article/pii/S0079661108000232 doi: https://doi.org/10.1016/j.pocean.2008.02.002
Lavers, D. A., & Villarini, G. (2013a). Atmospheric rivers and flooding over the central United States. *Journal of Climate*, *26*(20), 7829–7836. doi: 10.1175/JCLI-D-13-00212.1
Lavers, D. A., & Villarini, G. (2013b). The nexus between atmospheric rivers and extreme precipitation across Europe. *Geophysical Research Letters*, *40*(12), 3259–3264. doi: 10.1002/grl.50636
Li, C., & Wettstein, J. J. (2012). Thermally driven and eddy-driven jet variability in reanalysis. *Journal of Climate*, *25*(5), 1587–1596. doi: 10.1175/JCLI-D-11-00145.1
Lora, J. M., Mitchell, J. L., Risi, C., & Tripati, A. E. (2017). North pacific atmospheric rivers and their influence on western north america at the last glacial maximum. *Geophysical Research Letters*, *44*(2), 1051-1059. Retrieved from https://agupubs.onlinelibrary.wiley.com/doi/abs/10.1002/2016GL071541 doi: 10.1002/2016GL071541
Mundhenk, B. D., Barnes, E. A., & Maloney, E. D. (2016). All-Season Climatology and Variability of Atmospheric River Frequencies over the North Pacific. *Journal of Climate*, *29*(13), 4885–4903. Retrieved from https://doi.org/10.1175/JCLI-D-15-0655.1 doi: 10.1175/JCLI-D-15-0655.1
Neiman, P. J., Ralph, F. M., Wick, G. A., Lundquist, J. D., & Dettinger, M. D. (2008). Meteorological Characteristics and Overland Precipitation Impacts of Atmospheric Rivers Affecting the West Coast of North America Based on Eight Years of SSM/I Satellite Observations. *Journal of Hydrometeorology*, *9*(1), 22–47. doi: 10.1175/2007jhm855.1
Newell, R. E., Newell, N. E., Zhu, Y., & Scott, C. (1992). Tropospheric rivers? – a pilot study. *Geophysical Research Letters*, *19*(24), 2401-2404. Retrieved from https://agupubs.onlinelibrary.wiley.com/doi/abs/10.1029/92GL02916 doi: 10.1029/92GL02916
O'Brien, T. A., Collins, W. D., Rauscher, S. A., & Ringler, T. D. (2014). Reducing the computational cost of the ECF using a nuFFT: A fast and objective probability density estimation method. *Computational Statistics and Data Analysis*, *79*, 222–234. Retrieved from http://dx.doi.org/10.1016/j.csda.2014.06.002 doi: 10.1016/j.csda.2014.06.002
O'Brien, T. A., Kashinath, K., Cavanaugh, N. R., Collins, W. D., & O'Brien, J. P. (2016). A fast and objective multidimensional kernel density estimation method: FastKDE. *Computational Statistics and Data Analysis*, *101*, 148–160. Retrieved from http://dx.doi.org/10.1016/j.csda.2016.02.014 doi: 10.1016/j.csda.2016.02.014
O'Brien, T. A., Payne, A. E., Shields, C. A., Rutz, J., Brands, S., Castellano, C., . . . Zhou, Y. (2020). Detection Uncertainty Matters for Understanding Atmospheric Rivers. *Bulletin of the American Meteorological Society*(December), 790–796. doi: 10.1175/bams-d-19-0348.1

O'Brien, T. A., Risser, M. D., Loring, B., Elbashandy, A. A., Krishnan, H., Johnson, J., . . . Collins, W. D. (2020). Detection of atmospheric rivers with inline uncertainty quantification: Teca-bard v1.0. *Geoscientific Model Development Discussions*, *2020*, 1–20. Retrieved from `https://www.geosci-model-dev-discuss.net/gmd-2020-55/` doi: 10.5194/gmd-2020-55

Payne, A. E., & Magnusdottir, G. (2016). Persistent landfalling atmospheric rivers over the west coast of North America. *Journal of Geophysical Research*, *121*(22), 13,287–13,300. doi: 10.1002/2016JD025549

Price, G. R. (1972). Extension of covariance selection mathematics. *Annals of Human Genetics*, *35*(4), 485-490. Retrieved from `https://onlinelibrary.wiley.com/doi/abs/10.1111/j.1469-1809.1957.tb01874.x` doi: 10.1111/j.1469-1809.1957.tb01874.x

Ralph, F. M., & Dettinger, M. D. (2011, aug). Storms, floods, and the science of atmospheric rivers. *Eos, Transactions American Geophysical Union*, *92*(32), 265–266. Retrieved from `https://onlinelibrary.wiley.com/doi/abs/10.1029/2011EO320001` doi: 10.1029/2011EO320001

Ralph, F. M., Dettinger, M. D., Cairns, M. M., Galarneau, T. J., & Eylander, J. (2018, 05). Defining "Atmospheric River": How the Glossary of Meteorology Helped Resolve a Debate. *Bulletin of the American Meteorological Society*, *99*(4), 837-839. Retrieved from `https://doi.org/10.1175/BAMS-D-17-0157.1` doi: 10.1175/BAMS-D-17-0157.1

Ralph, F. M., Neiman, P. J., & Wick, G. A. (2004). Satellite and CALJET Aircraft Observations of Atmospheric Rivers over the Eastern North Pacific Ocean during the Winter of 1997/98. *Monthly Weather Review*, *132*(7), 1721–1745. Retrieved from `http://journals.ametsoc.org/doi/abs/10.1175/1520-0493{\%}282004{\%}29132{\%}3C1721{\%}3ASACAOO{\%}3E2.0.CO{\%}3B2` doi: 10.1175/1520-0493(2004)132<1721:SACAOO>2.0.CO;2

Ralph, F. M., Neiman, P. J., Wick, G. A., Gutman, S. I., Dettinger, M. D., Cayan, D. R., & White, A. B. (2006). Flooding on California's Russian River: Role of atmospheric rivers. *Geophysical Research Letters*, *33*(13), 3–7. doi: 10.1029/2006GL026689

Ralph, F. M., Rutz, J. J., Cordeira, J. M., Dettinger, M., Anderson, M., Reynolds, D., . . . Smallcomb, C. (2019, 03). A Scale to Characterize the Strength and Impacts of Atmospheric Rivers. *Bulletin of the American Meteorological Society*, *100*(2), 269-289. Retrieved from `https://doi.org/10.1175/BAMS-D-18-0023.1` doi: 10.1175/BAMS-D-18-0023.1

Ramos, A. M., Trigo, R. M., Liberato, M. L. R., & Tomé, R. (2015). Daily Precipitation Extreme Events in the Iberian Peninsula and Its Association with Atmospheric Rivers*. *Journal of Hydrometeorology*, *16*(2), 579–597. doi: 10.1175/jhm-d-14-0103.1

Rodean, H. C. (1996, 08). Stochastic Lagrangian Models of Turbulent Diffusion. *Meteorological Monographs*, *48*, 1-84. Retrieved from `https://doi.org/10.1175/0065-9401-26.48.1` doi: 10.1175/0065-9401-26.48.1

Rutz, J. J., Shields, C. A., Lora, J. M., Payne, A. E., Guan, B., Ullrich, P., . . . Viale, M. (2019). The atmospheric river tracking method intercomparison project (artmip): Quantifying uncertainties in atmospheric river climatology. *Journal of Geophysical Research: Atmospheres*, *124*(24), 13777-13802. Retrieved from `https://agupubs.onlinelibrary.wiley.com/doi/abs/10.1029/2019JD030936` doi: 10.1029/2019JD030936

Sawford, B. L. (1991). Reynolds number effects in lagrangian stochastic models of turbulent dispersion. *Physics of Fluids A: Fluid Dynamics*, *3*(6), 1577-1586. Retrieved from `https://doi.org/10.1063/1.857937` doi: 10.1063/1.857937

Sellars, S. L., Kawzenuk, B., Nguyen, P., Ralph, F. M., & Sorooshian, S. (2017). Genesis, Pathways, and Terminations of Intense Global Water Vapor Transport in Association with Large-Scale Climate Patterns. *Geophysical Research Letters*, *44*(24), 12,465–12,475. doi: 10.1002/2017GL075495

Shields, C. A., Rutz, J. J., Leung, L. Y., Martin Ralph, F., Wehner, M., Kawzenuk, B., . . .

Nguyen, P. (2018). Atmospheric River Tracking Method Intercomparison Project (ARTMIP): Project goals and experimental design. *Geoscientific Model Development*, *11*(6), 2455–2474. doi: 10.5194/gmd-11-2455-2018

Viale, M., Valenzuela, R., Garreaud, R. D., & Ralph, F. M. (2018). Impacts of Atmospheric Rivers on Precipitation in Southern South America. *Journal of Hydrometeorology*, *19*(10), 1671–1687. doi: 10.1175/jhm-d-18-0006.1

Waliser, D., & Guan, B. (2017). Extreme winds and precipitation during landfall of atmospheric rivers. *Nature Geoscience*, *10*(3), 179–183. doi: 10.1038/ngeo2894

Zhou, Y., & Kim, H. (2019). Impact of distinct origin locations on the life cycles of landfalling atmospheric rivers over the u.s. west coast. *Journal of Geophysical Research: Atmospheres*, *124*(22), 11897-11909. Retrieved from `https://agupubs.onlinelibrary.wiley.com/doi/abs/10.1029/2019JD031218` doi: 10.1029/2019JD031218

Zhou, Y., Kim, H., & Guan, B. (2018). Life cycle of atmospheric rivers: Identification and climatological characteristics. *Journal of Geophysical Research: Atmospheres*, *123*(22), 12,715-12,725. Retrieved from `https://agupubs.onlinelibrary.wiley.com/doi/abs/10.1029/2018JD029180` doi: 10.1029/2018JD029180

Zhu, Y., & Newell, R. E. (1998). A Proposed Algorithm for Moisture Fluxes from Atmospheric Rivers. *Monthly Weather Review*, *126*(3), 725–735. doi: 10.1175/1520-0493(1998)126<0725:apafmf>2.0.co;2